NASA's Hurricane and Severe Storm Sentinel (HS3) Investigation

Scott A. Braun, Paul A. Newman, Gerald M. Heymsfield

NASA Goddard Space Flight Center, Greenbelt, Maryland

Submitted to Bulletin of the American Meteor. Society

November 3, 2015

Revised

February 1, 2016

Corresponding author: Scott A. Braun, NASA Goddard Space Flight Center, Code 612, Greenbelt, MD 20771

Email: scott.a.braun@nasa.gov

Abstract

The National Aeronautics and Space Administration's (NASA) Hurricane and Severe Storm Sentinel (HS3) investigation was a multi-year field campaign designed to improve understanding of the physical processes that control hurricane formation and intensity change, specifically the relative roles of environmental and inner-core processes. Funded as part of NASA's Earth Venture program, HS3 conducted five-week campaigns during the hurricane seasons of 2012-14 using the NASA Global Hawk aircraft, along with a second Global Hawk in 2013 and a WB-57f aircraft in 2014. Flying from a base at Wallops Island, Virginia, the Global Hawk could be on station over storms for up to 18 hours off the East Coast of the U.S. to about 6 hours off the western coast of Africa. Over the three years, HS3 flew 21 missions over 9 named storms, along with flights over two non-developing systems and several Saharan Air Layer (SAL) outbreaks. This article summarizes the HS3 experiment, the missions flown, and some preliminary findings related to the rapid intensification and outflow structure of Hurricane Edouard (2014) and the interaction of Hurricane Nadine (2012) with the SAL.

A multi-year field campaign to measure environmental and inner-core processes that lead to storm formation and intensification into major hurricanes.

Almost 60 million Americans live within counties along the East and Gulf Coasts (140 million total in East and Gulf coast states), thus exposing them to the potential destruction caused by a landfalling hurricane. Societal vulnerability to damage has increased primarily because of growth in both population and wealth in coastal zones from Texas to Maine. Pielke et al. (2008) projected a doubling of economic losses from landfalling hurricanes every ten years. Advances in airborne and satellite observing systems, computing technologies, numerical models, and scientific understanding of hurricanes have led to significant advances in the understanding of hurricane motion and subsequent improvements in track prediction. However, improvements in prediction of storm intensity change have lagged due to an inadequate understanding of the processes that cause it, insufficient sampling of appropriate observations of the storm environment and internal processes, and inadequate representation of those processes in models (Rogers et al. 2006).

For five weeks in each of the hurricane seasons of 2012-2014, the National Aeronautics and Space Administration (NASA) conducted airborne campaigns using high-altitude long-duration Unmanned Airborne Systems (UASs) to investigate the processes that underlie hurricane formation and intensification. The Hurricane and Severe Storm Sentinel (HS3) mission, funded under NASA's Earth Venture program, comprised a set of aircraft and payloads well suited for the study of hurricanes and other severe weather systems. Using data from two Global Hawk (GH) UASs, the HS3 goal was to better understand the physical processes that control intensity

change, specifically the relative roles of environmental and inner-core processes. This goal was focused on the following science questions:

Environment:

1. What impact does the Saharan Air Layer (SAL) have on intensity change?
2. How do storms interact with shear produced by large-scale wind systems?
3. How does the outflow layer interact with the environment?

Inner core:

1. What is the role of deep convective towers (bursts) in intensity change? Are they critical to intensification?
2. What changes in storm structure occur prior to and during genesis and rapid intensification?
3. How do intrusions of dry air impact intensity change?

HS3 was designed to address these questions and to assess the impact, both in terms of research and applications, of remote and in-situ data sets from the Global Hawks on modeling and analysis. During its three deployments (Aug.-Sept. 2012, 2013, and 2014), HS3 obtained observations over 9 named storms during 21 flights, along with additional flights over SAL outbreaks and non-developing systems. HS3 demonstrated a key component of the observing system envisioned by MacDonald (2005) by bringing to bear the high-altitude long-endurance GH platform, a broad array of instruments, and new sampling strategies to provide data for in-depth study, for assimilation into models, and for detailed evaluation and validation of models.

AIRCRAFT

HS3 used two of NASA's unmanned GH aircraft [see Braun et al. (2013) for a background on the aircraft] and selected distinct payload sets for each aircraft. One GH, known as air vehicle one (AV-1) because it was the first GH ever built, was designated the "over-storm GH" since it carried three instruments specifically designed to measure the inner-core structure of storms. The second GH, known as AV-6, was designated the "environmental GH" because it carried instruments designed to characterize the storm environment including temperature, relative humidity, wind speed and direction, and profiles of Saharan dust. Unfortunately, due to engine and electrical issues, AV-1 was unable to deploy to the field in 2012 and 2014. In 2014, when it became clear that AV-1 would not deploy, the High-altitude Imaging Wind and Rain Airborne Profiler (HIWRAP) radar and Hurricane Imaging Radiometer (HIRAD) (see Braun et al. 2013 for descriptions) were moved onto the NASA Johnson Space Center WB-57f, which was conducting a coincident Office of Naval Research (ONR) Tropical Cyclone Intensity (TCI) mission utilizing a newly developed dropsonde system. The WB-57f is capable of flight durations up to 6 hours, a range of approximately 3700 km, and altitudes of approximately 18.3 km (60,000 ft). Three science missions were flown by the WB-57f, which deployed from McDill Air Force Base near Tampa, Florida.

HS3 PAYLOADS

The environmental GH carried three instruments, including the Scanning High-resolution Interferometer Sounder (S-HIS), Cloud Physics Lidar (CPL) and Airborne Vertical Atmospheric Profiling System (AVAPS).

S-HIS (details in Table 1; Revercomb 2015) is an advanced version of the HIS ER-2 instrument (Revercomb et al. 2003). Its noise levels are sufficiently low to allow cloud and surface properties to be derived from each individual field of view. Temperature and water vapor profiling can be performed on individual fields of view in the absence of significant clouds after taking advantage of Principal Component Analysis to reduce noise levels (Antonelli et al, 2004). The optical design is very efficient, providing useful signal-to-noise performance from a single 0.5-second dwell time. This allows imaging to be accomplished by cross-track scanning. Onboard reference blackbodies are viewed via a rotating 45° scene mirror as part of each cross-track scan, providing updated calibration information every 20-30 seconds.

CPL is a multi-wavelength backscatter lidar (McGill et al. 2002, 2003). CPL provides information on the radiative and optical properties of cirrus, subvisual cirrus clouds, and aerosols (McGill and Hlavka 2015). CPL utilizes a high-repetition rate, low-pulse energy transmitter and photon-counting detectors and measures the total (aerosol plus Rayleigh) attenuated backscatter as a function of altitude at each wavelength. For transmissive cloud/aerosol layers, the extinction-to-backscatter parameter (S-ratio) can be directly derived using optical depth measurements determined from attenuation of Rayleigh and aerosol scattering and using the integrated backscatter. This permits unambiguous analysis of cloud optical depth since only the lidar data is required. Using the derived extinction-to-backscatter ratio, the internal cloud extinction profile can then be obtained (McGill et al 2003).

The AVAPS dropsonde system has been used for hurricane research since the late 1990's (Hock and Franklin 1999; Halverson et al. 2006). Dropsondes provide in-situ, high-vertical resolution profiles of basic atmosphere state variables – temperature, pressure, humidity, location, and winds (Wick 2015). The GH dropsonde system was developed and built by the

National Center for Atmospheric Research (NCAR) and carries up to 88 dropsondes per flight. It is the first aircraft dropsonde system with full remote operation. In 2012, AVAPS experienced significant radio frequency interference (RFI) from other AV-6 systems, resulting in loss of data within some dropsonde profiles. The lowest levels were most frequently impacted. The RFI issues were resolved for the 2013 and 2014 campaigns where the dropsonde data from the aircraft to the ocean surface was good and AVAPS also provided good data for the NOAA Winter Storms and Pacific Atmospheric Rivers (WISPAR, Neiman et al. 2014) program in 2011.

The over-storm payload consisted of the High-altitude Atmospheric Monolithic Microwave Integrated Circuits Sounding Radiometer (HAMSR), HIWRAP, and HIRAD. A description of these instruments can be found in Braun et al. (2013).

SUMMARY OF HS3 FLIGHTS

During the 3 years of deployments, HS3 flew 670 total flight hours and released 1426 dropsondes, including full 88-dropsonde loads on two flights (19-20 Sept. 2013 and 16-17 Sept. 2014). The GH flew 18 flights over 8 named storms over 3 years while the WB-57f flew 3 flights over Hurricane Gonzalo in 2014 (Table 2).

In addition, the GH flew 2 non-developing systems (19-20 Sept. 2013 and 5-6 Sept. 2014) that the National Hurricane Center (NHC) predicted had some potential to develop, 2 flights specifically targeting the SAL (20-21 and 24-25 Aug., 2013), and 2 broad surveys of the Atlantic Main Development Region (MDR) (22-23 and 28-29 Sept., 2014). Several additional flights focused on instrument inter-comparisons. The 8-9 Sept. 2011 flight sampled an atmospheric river event and was designed to inter-compare temperature and humidity profiles from AVAPS, HAMSR, and S-HIS. The 13-14 Sept. 2011 and 30 Sept. 2014 flights were designed to compare measurements from GH and National Oceanic and Atmospheric Administration (NOAA) G-IV

dropsondes. The 25 Sept. 2013 flight sampled precipitation in a mid-latitude frontal system to compare measurements from the HIWRAP (GH) and IWRAP (NOAA P-3) radars. Flight tracks for all flights, excluding the instrument inter-comparison and test flights, are shown in Fig. 1.

The most significant storms of the campaign were hurricanes Nadine (2012), Edouard (2014), and Gonzalo (2014). Hurricane Nadine and Tropical Storm Gabrielle were the only tropical cyclones to involve significant SAL interactions. Edouard and Gonzalo were the only major hurricanes to occur during the 3 deployments. Hurricane Cristobal was sampled during its extratropical transition.

SCIENCE HIGHLIGHTS

A number of future studies will provide detailed analyses of the observations obtained during HS3. This section provides highlights of notable events and unique opportunities for research enabled by the HS3 mission. The highlights include a period of apparent rapid intensification (RI) not noted in the final NHC Tropical Cyclone Report for Hurricane Edouard, eyewall replacement cycles in Hurricane Gonzalo, SAL interaction with Hurricane Nadine, and unprecedented storm outflow measurements.

Abrupt intensity changes in Hurricane Edouard (2014)

Four flights were conducted over Hurricane Edouard's lifecycle (11-19 Sept. 2014), including an abrupt intensification on 14 September 2014. Although Edouard fell just short of the 24-hour intensity change (best-track value, 12.9 m s^{-1}; RI threshold, 15.4 m s^{-1}) typically associated with RI (Kaplan and DeMaria 2003), HS3 and satellite observations suggest that Edouard underwent a period of significant intensification during the 9-hour period from 15 UTC

14 September to 00 UTC 15 September followed by weakening during an eyewall replacement cycle. Key measurements from the first two flights are described below.

Figure 2 highlights the ability of the GH to provide extensive coverage of the storm environment as well as repeated overflights of the inner core during the 24-26 hour flights. During HS3's first Edouard flight on 12 September (Figs. 2a-c), the GH was on station from approximately 0430 to 1430 UTC. Edouard, then a tropical storm with maximum winds ~18-21 m s^{-1} (35-40 kt), was experiencing moderate southwesterly vertical wind shear (~9 m s^{-1})[1], leading to a highly asymmetric cloud structure. The 800-hPa circulation (Fig. 2a) was centered on a region of intense convection in a relatively moist environment (>70%, orange and red filled circles). At 400 hPa (Fig. 2b), strong west-northwesterly storm-relative flow brought very dry air over the southern portion of the storm (blue filled circles), and the center of circulation was displaced ~200 km to the northeast (downshear) of the low-level center in a region of stratiform precipitation. A well-defined outflow jet at 200 hPa (Fig. 2c) was evident on the northern side of the storm with anticyclonic flow near the center. Temperatures at 200 hPa (Fig. 2c) just south of the deep convection suggest warming of 3 K (cyan color) relative to the surrounding environment (dark blue color).

During the 14-15 September flight (Figs. 2d-f), the GH was on-station for almost 19 hours. The vertical shear decreased slightly to 7 m s^{-1} from the southeast at 18 UTC 14 September[2] while Edouard became vertically aligned (Fig. 2d-e). Dry environmental air was present at mid-to-upper levels (Fig. 2e) in this sheared environment, conditions that might be expected to inhibit

---

[1] Deep-layer shear (850-200 hPa) from the Statistical Hurricane Intensity Prediction System (SHIPS, DeMaria and Kaplan 1994, 1999; DeMaria et al. 2005) from an analysis with the hurricane vortex removed and averaged from the center to a radius of 500 km at 12 UTC 12 September.

[2] SHIPS shear values increased after this time.

or slow intensification (Tao and Zhang 2014). Despite these conditions, Edouard quickly intensified to 41 m s^{-1} (80 kt) by 0000 UTC 15 September according to the NHC final report (Stewart, 2014). A broad 200 hPa outflow jet developed on the western side of the storm (Fig. 2f) while maintaining a well-defined cyclonic circulation close to the center with temperatures ~9 K warmer than the surrounding environment.

Evidence of abrupt intensification and weakening of Edouard during the period of the GH flight is seen in GOES satellite imagery (Fig. 3) and NOAA P-3 and GH dropsondes. Table 3 summarizes data from 5 dropsondes released in the vicinity of the eye or inner edge of the eyewall during the period from 1500 UTC 14 September to 0430 UTC 15 September. All of the dropsondes, except the first P-3 drop, measured strong near-surface winds up to 41 m s^{-1}, suggesting that the dropsondes entered the region near the low-level eyewall before reaching the surface and that the central pressure was much lower than the measured surface pressure. Notable observations early in the period include:

- 0845 UTC: An initial eye became apparent in GOES infrared imagery (not shown).
- 1115-1515 UTC: A convective burst developed on the northwestern side of the eye (Fig. 3a), obscuring the eye as its cloud shield wrapped around to the eastern side of the circulation (Fig. 3b).
- 1500 UTC: A NOAA P-3 dropsonde measured a central pressure of 983 hPa. NOAA P-3 tail Doppler radar data (Fig. 4a) showed strong winds in the northeastern quadrant of the storm with a radius of maximum winds of ~25 km. A weak secondary wind speed maximum was seen in the same quadrant close to 50 km radius. Precipitation was very asymmetric with the heaviest precipitation in the southwestern eyewall associated with the convective burst.

- 1707 UTC: A P-3 dropsonde on the inner edge of the northeastern eyewall measured a surface pressure of 984 hPa and a 10-m wind of 37 m s^{-1}. The strong 10-m wind suggests a much lower central pressure at this time. A new, very small eye formed in the GOES imagery near this time (not shown), suggesting the onset of upper-level descent in the eye.

During the period when Edouard had a very small eye (1715-0215 UTC), the GH released 2 dropsondes in the eye that entered the eyewall at low levels on the northern side of the eyewall. The first GH center transect was a north-to-south pass, with the eye overflight occurring near 2104 UTC 14 September (Fig. 3d). GOES IR imagery showed a very small eye with the GH passing between two regions of higher cloud-top heights (inferred from the colder cloud-top temperatures) associated with deep convection. S-HIS Brightness temperatures (Fig. 5a) indicate that the 2104 UTC dropsonde was released on the eastern side of the eye, with the dropsonde gradually moving around to the northern eyewall at low levels. This dropsonde measured a surface pressure of 972 hPa and an estimated 10-m wind speed of 41 m s^{-1} (80 kt).

Although GOES imagery suggested significant axisymmetrization of the upper-level cloud field during this intensification period, the storm circulation remained highly asymmetric, consistent with the moderate vertical wind shear that continued at this time. Figure 5b shows a vertical cross section of storm-relative tangential[3] winds obtained from dropsondes along this north-to-south flight leg, with the 2104 UTC dropsonde closest to the storm center. The dropsonde spacing in the inner-core region was insufficient to resolve the eyewall and eye, but

[3] The center location was estimated from the warm S-HIS brightness temperatures in the clear eye and the trajectory of the 2104 UTC dropsonde (see Fig. 5a). Radial and tangential winds within ~1° radius are sensitive to the center position estimate and should be viewed with some caution, while values outside of 1° are not very sensitive.

the figure clearly shows the strong tangential winds on both the northern and southern sides of the center. Strong radial inflow (Fig. 5c) occurred in the boundary layer on the northern side of the storm while weak outflow was present south of the center. A prominent outflow jet was present in the 8.5-15 km altitude layer to the north of the center, while weaker outflow near 11 km altitude occurred to the south, consistent with the 200-hPa wind analysis in Fig. 2f. Dry air (Fig. 5d) was located about 2° (~220 km) to the south and 3° (~330 km) to the north of the center of the storm[4].

During the second center overflight at 0032 UTC 15 September (see GOES imagery for 0045 UTC in Fig. 3d), a dropsonde released in the upper eye fell into the northern eyewall at low levels, measuring a surface pressure of 967 hPa and a near-surface wind speed of 38 m s^{-1} (74 kt). Figure 6 shows the timing of the 0032 UTC dropsonde relative to the cloud attenuated backscatter from CPL and real-time temperatures from S-HIS. The 0032 UTC dropsonde was clearly released into the eye and the CPL (Fig. 6) and dropsonde data (not shown) both suggest that the dropsonde entered the inner edge of the eyewall near 800 hPa.

Edouard's small eye persisted continuously in GOES imagery until 0215 UTC, after which the cloud structure gradually became more disorganized (Fig. 3e), suggesting a reorganization of the eyewall. TRMM rainfall data from the precipitation radar and microwave imager at 0044 UTC 15 September (Fig. 4b) suggest an asymmetric inner eyewall at a radius close to the radius of maximum wind seen in the earlier P-3 Doppler analysis (Fig. 4a), and another ring of rainfall with a radius of ~50 km that is close to the radius of the secondary wind maximum seen earlier, consistent with the onset of an eyewall replacement cycle. By 0900 UTC, a new eye reformed in

[4] Comparisons between S-HIS and AVAPS suggest a dry bias in the AVAPS data above 400 hPa, so relative humidities with respect to ice above ~8 km should be closer to saturation within the cloud system.

the upper-level clouds (shown in Fig. 3f at 1345 UTC), but with a radius about 4-5 times larger than seen earlier (Fig. 3c). The last GH dropsonde near the center at 0428 UTC measured a pressure of 971 hPa and 10-m wind of 39 m s^{-1} (76 kt) in the northern eyewall area, suggesting a weakened intensity coincident with the apparent eyewall replacement cycle.

While there is no direct way to estimate the storm central pressure from a dropsonde near the eyewall, we can estimate the range of central pressures using Holland (1980). Holland's Eq. (3) can be solved for the central pressure,

$$p_c = \frac{p_r - p_e e^{\emptyset}}{1 - e^{\emptyset}}$$

where p_c is the central pressure, p_r is the pressure at radius r, p_e is an environmental pressure (taken here as the first open isobar on a surface pressure analysis). The parameter $\emptyset = -(R_m/r)^B$, where R_m is the radius of maximum wind, and $B = e\rho V_m^2/(p_e - p_c)$, e is the base of natural logarithms, ρ is the density of air, and V_m is the maximum wind speed. For calculations of p_c, the following values are assumed: p_e=1016 hPa, ρ =1.15 kg m^{-3}, and V_m=40 m s^{-1}. Using the Doppler analysis in Fig. 4a, R_m is estimated to be ~25 km. Given uncertainty of the storm center position, the dropsonde radial locations are estimated to be between 10-20 km. The equations for B and p_c are solved iteratively for radii of 10, 15, and 20 km.

Figure 7 shows the resulting central pressure estimates (blue lines) for the three radii for each dropsonde along with the NHC best-track central pressure and operational intensity estimates (Stewart 2014). It should be noted that the NHC best-track record is a subjectively smoothed representation of the storm's intensity that does not attempt to resolve intensity variations smaller than 24 hours (James Franklin, personal communication). The aircraft data, combined with the GOES imagery, suggest significant intensity variations on much shorter time scales than resolved in the best-track record. The data suggest that abrupt

intensification occurred as the central pressure decreased from 983 to 962 hPa, and possibly much lower, but quickly came to an end as a result of an eyewall replacement cycle. The estimated central pressures from the GH dropsondes are consistent with some of the satellite-based central pressure estimates (red dots) between 1700 UTC 14 September and 0600 UTC 15 September, with the exception of the 0032 UTC GH dropsonde, which is much lower. Although the best-track intensity at 00 UTC 15 September was set to 41 m s^{-1}, individual satellite-derived estimates of maximum wind speed near that time exceeded 46 m s^{-1} [Fig. 2 of Stewart (2014)], which appears to be consistent with the abrupt intensification indicated by the dropsondes.

The abrupt intensity changes suggested by the Edouard data are reminiscent of those in Gabrielle (2001) (Molinari et al. 2006, Molinari and Vollaro 2010) and Claudette (2003) (Shelton and Molinari 2009), but with some notable differences. Both Gabrielle and Claudette remained weak for several days after their abrupt intensity changes, were characterized by much greater asymmetry in cloud structure, and vertical shear was a key factor in their weakening . In contrast, Edouard's overall trend was toward greater intensity, the GOES cloud signature was much more symmetric, and the brief weakening was caused by an eyewall replacement cycle.

Tropical Cyclone-SAL interaction (Nadine)

Hurricane Nadine (2012) was HS3's best case for examining the interaction of a tropical cyclone with the SAL. Nadine originated from a tropical wave that emerged from the West African coast on 7 September in association with a small dust outbreak to its north. As the wave moved westward on 9 September, a large and more intense dust outbreak exited the Sahara and advanced toward the tropical disturbance. Nadine became a tropical depression on 10 September

(Fig. 8a) and by 11 September (Fig. 8b) the SAL outbreak was encroaching on the cloud system's northern and eastern sides. Nadine became a tropical storm at 0000 UTC 12 September during the middle of the first GH flight. Dropsonde data were collected in the western part of the storm, but were discontinued midway through the flight after a dropsonde became jammed in the launcher. As a result, no dropsondes were obtained in the eastern part of the storm and within the SAL.

Neither dropsonde nor CPL data indicated the presence of SAL air in the northwestern quadrant of the storm during the 11-12 September flight (northern portions of the 2nd and 3rd flight legs from the left on the western side of the storm in Fig. 8b). With dropsondes disabled, CPL and S-HIS detected a deep layer of SAL air (Fig. 9) along the northern portions of the 4th and 5th flight legs in Nadine's northeastern quadrant. Upon traversing north of Nadine's upper cloud shield (~0100 UTC, Fig. 9a), CPL detected a deep dust layer with a top near 530 hPa. In the dust region, S-HIS retrievals (Fig. 9b) indicated very hot (perturbations of +6-9 K) and dry (0-20% relative humidity) air between 850-700 hPa and cooler and more moist conditions (~50%) near the top of the dust layer, consistent with Carlson and Prospero (1972), Messager et al. (2009), Ismail et al. (2010), and Braun (2010).

The 14-15 September flight occurred as Nadine was moving northward near 54°W with the SAL encroaching on its eastern and northern sides (Fig 8c-e). Vertical shear estimates from SHIPS (DeMaria and Kaplan 1994, 1999; DeMaria et al. 2005) indicated 850-200 hPa vertical wind shear (not shown) changing from weak northwesterly shear on 12 September to west-southwesterly shear of 12-15 m s^{-1} by 0000 UTC 15 September. During the period of weak shear on 12 September, Nadine intensified 12.9 m s^{-1} in 24 hours, 2.6 m s^{-1} below the threshold for rapid intensification (Kaplan and DeMaria 2003). With the onset of stronger vertical shear on 13

September, negligible intensification occurred from 0000 UTC 13 to 1200 UTC 14 September. A series of convective bursts with coincident frequent lightning during the GH flight between 1400-2100 UTC 14 September likely helped Nadine intensify (Steranka et al. 1986; Kelley et al. 2004; Guimond et al. 2010; Stevenson et al. 2014; Rogers et al. 2015) to hurricane intensity by 1800 UTC 14 September before strong environmental westerlies pushed Nadine quickly eastward over cooler waters.

Global Hawk dropsonde observations of equivalent potential temperature (θ_e) and storm-relative winds spanning the period 17 UTC 14 September to 08 UTC 15 September are shown in Fig. 10. At 800 hPa (Fig. 10a), low θ_e air associated with the SAL is found on the eastern side of the storm wrapping around the northern side, consistent with MODIS observations over preceding days, with a principal rainband marking the boundary between SAL in the outer environment and more moist conditions in the inner core. The dry SAL air is on the downshear side of the storm. The shear-related storm-relative inflow on the downshear side (Bender 1997; Braun et al. 2006) may have fostered a pathway for SAL air into the inner-core circulation there (Willoughby et al. 1984; Marks et al. 1992; Braun et al. 2006; Riemer and Montgomery 2011). At 400 hPa (Fig. 10b), very dry westerly flow associated with the strong environmental shear impinged on the entire western flank of the storm, with the driest air wrapping around the southern side of the circulation. It is not yet possible to determine the impact of the SAL and upper-level dry air from these observations. However, ensemble simulations with the Weather Research and Forecasting model with coupled aerosol-cloud-radiation physics are being used to quantify the role of the SAL and dry air in this case.

Tropical cyclone outflow structure

Tropical cyclone outflow is a prominent part of the secondary circulation and its thermodynamic structure plays a key role in hurricane maximum potential intensity (MPI) theory. Emanuel (1986, 1997) derived expressions for MPI in an axisymmetric framework that depended on a constant outflow temperature with the outflow occurring above the tropopause (Emanuel and Rotunno 2011). The model assumed that outflow streamlines asymptotically approach altitudes at which their saturated entropy values match those of the undisturbed environment so that outflow structure is determined by environmental stratification. However, Emanuel and Rotunno (2001) used simulated storms to demonstrate that outflow stratification is instead the result of internal dynamics and small-scale turbulence that limits the Richardson number (*Ri*) to a critical value needed for the onset of that turbulence.

Molinari et al. (2014) examined NOAA G-IV dropsonde data and identified three situations that produce low *Ri* in outflow regions. The first situation was just beneath the outflow-layer stratiform cloud deck where sublimation cooling produced high stability near cloud base and a neutral or unstable lapse rate and low *Ri* just beneath the stable layer. In the second case, low *Ri* occurred above cloud base where radiative heating (cooling) near cloud base (top) resulted in sufficiently low stability to cause low *Ri* values. Vertical wind shear was not a contributor to the low *Ri* in either of these cases. The third situation occurred outside the central dense overcast in association with strong vertical wind shear at the base of the outflow layer.

The G-IV dropsondes typically provide data only below 12-13 km and therefore miss the upper part of the outflow layer and the lower stratosphere. During HS3, the GH provided relatively high-density coverage over a large extent of the outflow layer from the lower stratosphere to the surface. An example of outflow layer structure was shown in Fig. 5. To the

north of the center, outflow >4 m s^{-1} extended vertically between ~8.5 to 15 km and from the eyewall to more than 8° (~770 km) from the center. The strongest outflow occurred just beneath cloud top near the northern eyewall, but beyond a radius of ~200 km, outflow often extended above and beyond regions of cloudiness. In addition to inflow beneath the outflow layer, another region of strong inflow existed in the lower stratosphere above the outflow layer and extended all the way inward to the storm center. Tangential velocities in the outflow layer transitioned from cyclonic flow beneath cloud top out to ~28°N (~250 km radius) to strong anticyclonic flow northward of 30°N (~400 km radius). A very shallow layer of strong anticyclonic velocities occurred at the tropopause at the transition from upper-tropospheric outflow to lower-stratospheric inflow.

Figure 11 shows results from a calculation of the Richardson number using the data shown in Fig. 5. In unsaturated regions (taken here as regions with relative humidity < 95%), *Ri* is estimated from $Ri = N^2/S^2$, where $N^2 = (g/\theta_v)(\Delta\theta_v/\Delta z)$, $S^2 = [(\Delta U)^2 + (\Delta V)^2]/(\Delta z)^2$, θ_v is the virtual potential temperature, *U* and *V* are the zonal and meridional wind components, respectively, and *z* is geopotential height. Where relative humidity > 95%, a moist *Ri* [Eqs. A1-A4 of Molinari et al (2014)] derived from Durran and Klemp (1982) is used. Very low moist-*Ri* values are found in the inner core below 6 km associated with both low stability (N^2, Fig. 11b) and moderate shear (*S*, Fig. 11c). A region of low *Ri* (<1) is found above the outflow layer just above the tropopause and is characterized by very strong shear and relatively higher stability (*N* of 0.01–0.025 s^{-1}). Within this layer, a shallow layer is associated with *Ri*<0.25 where *N*~0.01 s^{-1}. This lower stratospheric layer of low *Ri,* and the transition into the outflow layer, would not be detectable from G-IV dropsondes because of their lower release altitude. The dropsonde profiles near 23.7° (at 6- and 7.5-km altitude) and 29.7°N (at 7 km) exhibit sublimation-induced unstable

layers a few hundred meters in depth associated with intrusions of dry air beneath cloud base at mid levels similar to that seen by Molinari et al. (2014). Within the outflow layer, some regions with $Ri<1$ are found, particularly near the northern eyewall, and are often associated with low stability in the outflow layer. However, unlike in Molinari et al. (2014), moderate vertical wind shear usually also contributes significantly to the low *Ri* values there.

SUMMARY

Along with the NASA GRIP campaign, HS3 has demonstrated the unique contributions of the Global Hawk for conducting hurricane science research, taking advantage of the long duration, high altitude, and heavy payload capabilities of the aircraft. While GRIP produced the first-ever GH flights, the GH was launched from NASA's Armstrong Flight Research Center in Southern California, which greatly reduced on-station times for storms eastward of the Gulf of Mexico and prevented flights east of about 66°W. HS3 paved the way for flights from the East Coast and demonstrated the use of mobile trailers for controlling the GH and its payload. These East Coast deployments allowed flights over extended periods of most storm systems in the Atlantic, particularly for storms not accessible by operational manned aircraft. Flight patterns for the UAS could be adjusted in real-time to account for changing storm conditions.

The observations collected by the environmental GH (AV-6) will help address HS3's environmental science questions related the interaction of storms with vertical shear and the Saharan Air Layer, as well as the structure and role of the outflow layer. Because of the problems with the over-storm GH (AV-1), addressing the inner-core science questions will require combining available AV-6 and WB-57f data with information from NOAA aircraft and satellites, as well as numerical models. Along with several tropical cyclones, HS3 obtained data

useful for the study of the structure of the SAL and environmental processes in two non-developing systems.

Over the course of the HS3 mission, NASA developed key relationships with NOAA, the Federal Aviation Administration, and Department of Defense to implement and improve operational procedures and demonstrate the scientific value of the GH data sets, leading to efforts by NOAA's Sensing Hazards with Operational Unmanned Technologies (SHOUT) program to examine the operational forecasting utility of the GH platform and instruments.

The HS3 mission web page is https://espo.nasa.gov/hs3. The HS3 data archive is at https://ghrc.nsstc.nasa.gov/HS3.html.

Acknowledgements

We thank James Franklin, Robert Rogers, and an anonymous reviewer for their very helpful reviews. Paul Reasor and Robert Rogers provided the P-3 dual-Doppler radar data used in Figure 4. NOAA P-3 dropsonde data were provided by NOAA's Physical Oceanography Division (PHOD) of Atlantic Oceanographic and Meteorological Laboratory. Dennis Hlavka and John Yorks from Goddard provided the CPL data. Peter Black, James Doyle, and Jon Moskaitis provided valuable discussions related to storm outflow. The HS3 mission was funded by NASA's Earth Venture Suborbital program at NASA Headquarters.

Sidebar: Inner-Core Structure During Hurricane Gonzalo.

The three flights of the WB-57f over Hurricane Gonzalo (Fig. 1d and Table 2) provided inner-core measurements during an interesting period when the storm was moving northwestward and then north-northeastward around a ridge in the central Atlantic. The storm intensified from category 3 on 15 October to category 4 on 16 October, when it had a minimum central pressure of 940 hPa and maximum winds of 125 kt. An eyewall replacement cycle occurred on the 15th, causing the storm to weaken briefly before recurving. Gonzalo again had a double eyewall late on 16 October, also concurrent with a weakening of the storm.

Figure S1 shows the HIWRAP (Heymsfield 2015) reflectivity structure highlighting the double eyewall structure on 17 September 2014. Gonzalo had an asymmetrical structure with its cloud shield spreading to the north and east. The heavier precipitation in the cross section is on the northwest side of the storm. This cross section and other similar passes over the three days are being analyzed for both precipitation and wind structure similar to what has been done in previous HIWRAP studies (Guimond et al. 2014; Didlake et al. 2014).

References

Morris A. Bender, 1997: The Effect of Relative Flow on the Asymmetric Structure in the Interior of Hurricanes. *J. Atmos. Sci.*, **54**, 703–724.

Braun, S. A., 2010: Re-evaluating the role of the Saharan Air Layer in Atlantic tropical cyclogenesis and evolution. *Mon. Wea. Rev.*, **138**, 2007-2037.

Braun, S. A., M. T. Montgomery, and Z. Pu, 2006: High-Resolution Simulation of Hurricane Bonnie (1998). Part I: The Organization of Vertical Motion. *J. Atmos. Sci.,* **63**, 19-42.

Braun, S. A., and coauthors, 2013: NASA's Genesis and Rapid Intensification Processes (GRIP) Field Experiment. *Bull. Amer. Meteor. Soc.*, **94**, 345-363.

Carlson, T.N., and J.M. Prospero, 1972: The large-scale movement of Saharan air outbreaks over the northern equatorial Atlantic. *J. Appl. Meteor.*, **11**, 283-297.

DeMaria, M., and J. Kaplan, 1994: A Statistical Hurricane Intensity Prediction Scheme (SHIPS) for the Atlantic basin. *Wea. Forecasting*, **9**, 209–220.

DeMaria, M., and J. Kaplan, 1999: An updated statistical hurricane intensity prediction scheme (SHIPS) for the Atlantic and eastern North Pacific Basins. *Wea. Forecasting*, **14**, 326-337.

DeMaria, M. M. Mainelli, L. K. Shay, J. A. Knaff, and J. Kaplan, 2005: Further Improvements to the Statistical Hurricane Intensity Prediction Scheme (SHIPS). *Wea. Forecasting*, **20**, 531-543.

Didlake, A. C., Jr., G. M. Heymsfield, L. Tian, and S. R. Guimond, 2015: The coplane analysis technique for three-dimensional wind retrieval using the hiwrap airborne doppler radar. *J. Appl. Meteor. Climatol.*, **54**, 605–623. doi: http://dx.doi.org/10.1175/JAMC-D-14-0203.1

Durran, D. R., and J. B. Klemp, 1982: On the effects of moisture on the Brunt-Väisälä

frequency. *J. Atmos. Sci.*, **39**, 2152–2158

Emanuel K. A., 1986: An air–sea interaction theory for tropical cyclones. Part I: Steady-state maintenance. *J. Atmos. Sci.*, **43**, 585–604.

Emanuel, K. A., 1997: Some aspects of hurricane inner-core dynamics and energetics. *J. Atmos. Sci.*, **54**, 1014–1026.

Emanuel, K. A., and R. Rotunno, 2011: Self-stratification of tropical cyclone outflow. Part I: Implications for storm structure. *J. Atmos. Sci.*, **68**, 2236–2249, doi:10.1175/JAS-D-10-05024.1.

Guimond, S. R., G. M. Heymsfield, and F. J. Turk, 2010: Multiscale Observations of Hurricane Dennis (2005): The Effects of Hot Towers on Rapid Intensification. *J. Atmos. Sci.*, **67**, 633–654.

Guimond, S. R., L. Tian, G. M. Heymsfield, and S. J. Frasier, 2014: Wind retrieval algorithms for the IWRAP and HIWRAP airborne Doppler radars with applications to hurricanes. *J. Atmos. Oceanic Technol.*, **31**, 1189-1215.

Halverson, J. B., J. Simpson, G. Heymsfield, H. Pierce, T. Hock, and L. Ritchie, 2006: Warm core structure of Hurricane Erin diagnosed from high-altitude dropsondes during CAMEX-4. *J. Atmos. Sci.*, **63**, 309-324.

Heymsfield, Gerald H. 2015. Hurricane and Severe Storm Sentinel (HS3) High Altitude Imaging Wind and Rain Airborne Profiler (HIWRAP). Dataset available online [https://hs3.nsstc.nasa.gov/pub/hs3/HIWRAP/] from the NASA Global Hydrology Resource Center DAAC, Huntsville, Alabama, U.S.A. http://dx.doi.org/10.5067/HS3/HIWRAP/DATA101

Hock, T., and J. L. Franklin, 1999: The NCAR GPS dropwindsonde. *Bull. Amer. Meteor. Soc.*,

80, 407–420.

Holland, G. J., 1980: An analytic model of the wind and pressure profiles in hurricanes. *Mon. Wea. Rev.*, **108**, 1212-1218.

Ismail, S., and coauthors, 2009: LASE measurements of water vapor, aerosol, and cloud distributions in Saharan air layers and tropical disturbances. *J. Atmos. Sci.*, **67**, 1026-1047.

Kaplan, J., and M. DeMaria, 2003: Large-scale characteristics of rapidly intensifying tropical cyclones in the North Atlantic basin. *Wea. Forecasting*, **18**, 1093-1108.

Kelley, O. A., J. Stout, and J. B. Halverson, 2004: Tall precipitation cells in tropical cyclone eyewalls are associated with tropical cyclone intensification. *Geophys. Res. Letters*, **31**, L24112, doi:10.1029/2004GL021616.

MacDonald, A. E., 2005: A global profiling system for improved weather and climate prediction. *Bull. Amer. Meteor. Soc.*, **86**, 1747-1764.

Marks, F. D., Houze, R. A., and Gamache, J. F., 1992: Dual-aircraft investigation of the inner core of Hurricane Norbert. Part I: Kinematic structure, *J. Atmos. Sci.*, **49**, 919–942.

McGill, Matthew and Dennis Hlavka. 2015. Hurricane and Severe Storm Sentinel (HS3) Global Hawk Cloud Physics Lidar (CPL) [ATB files]. Dataset available online [https://hs3.nsstc.nasa.gov/pub/hs3/CPL/] from the NASA Global Hydrology Resource Center DAAC, Huntsville, Alabama, U.S.A. doi: http://dx.doi.org/10.5067/HS3/CPL/DATA202.

McGill, M., D. Hlavka, W. Hart, V. S. Scott, J. Spinhirne, and B. Schmid, 2002: Cloud Physics Lidar: Instrument Description and Initial Measurement Results. *Appl. Opt.*, **41**, 3725-3734.

McGill M., L. Li, W. D. Hart, G. M. Heymsfield, D. L. Hlavka, P. E. Racette, L. Tian, M. A. Vaughan, and D. M. Winker, 2003: Combined lidar–radar remote sensing: Initial results from CRYSTALFACE. *J. Geophys. Res.*, **109**, D07203, doi: 10.1029/2003JD004030.

Messager, C., D. J. Parker, O. Reitebuch, A. Agusti-Panareda, C. M. Taylor, and J. Cuesta, 2009: Structure and dynamics of the Saharan atmospheric boundary layer during the West African monsoon onset: Observations and analyses from the research flights of 14 and 17 July 2006. *Quart. J. Roy. Meteor. Soc.*, **135**, doi:10.1002/qj.469.

Molinari, J., and D. Vollaro, 2010: Rapid intensification of a sheared tropical storm. *Mon. Wea. Rev.*, **138**, 3869-3885.

Molinari, J., P. Duran, and D. Vollaro, 2014: Low Richardson Number in the Tropical Cyclone Outflow Layer. *J. Atmos. Sci.*, **71**, 3164-3179.

Molinari, J., P. Dodge, D. Vollaro, K. Corbosiero, and F. Marks Jr., 2006: Mesoscale aspects of the downshear reformation of a tropical cyclone. *J. Atmos. Sci*, **63**, 341-354.

Neiman P. J., G. A. Wick, B. J. Moore, F. M. Ralph, J. R. Spackman and B. Ward, 2014: An Airborne Study of an Atmospheric River over the Subtropical Pacific during WISPAR: Dropsonde Budget-box Diagnostics, and Precipitation Impacts in Hawaii. *Mon. Wea. Rev.*, **142**, 3199-3223. doi:10.1175/MWR-D-13-00383.1

Pielke, R. A., J. Gratz, C. W. Leadsea, D. Collins, M. A. Saunders, and R. Musulin, 2008: Normalized hurricane damages in the United States: 1900–2005. *Natural Hazards Review*, **9**, 29-42.

Revercomb, Henry. 2015. Hurricane and Severe Storm Sentinel (HS3) Scanning High-Resolution Interferometer Sounder (S-HIS)). Dataset available online [https://hs3.nsstc.nasa.gov/pub/hs3/SHIS/] from the NASA Global Hydrology Resource

Center DAAC, Huntsville, Alabama, U.S.A. doi: http://dx.doi.org/10.5067/HS3/SHIS/DATA201.

Revercomb, H. E., and coauthors, 2003: Applications of high spectral resolution FTIR observations demonstrated by radiometrically accurate ground-based AERI and Scanning HIS aircraft instruments. SPIE Proceedings Multispectral and Hyperspectral Remote Sensing Instruments and Applications, *Proc. SPIE*, 4897, **11**; doi:10.1117/12.466834, 11–23.

Riemer, M., and M. T. Montgomery, 2011: Simple kinematic models for the environmental interaction of tropical cyclones in vertical wind shear. *Atmos. Chem. Phys.*, **11**, 9395–9414, doi:10.5194/acp-11-9395-2011.

Rogers, R., and coauthors, 2006: The Intensity Forecasting Experiment: A multi-year field program for improving tropical cyclone intensity forecasts. *Bull. Amer. Meteor. Soc.*, **87**, 1523-1537.

Rogers, R. F., P. D. Reasor, and J. A. Zhang, 2015: Multiscale Structure and Evolution of Hurricane Earl (2010) during Rapid Intensification. *Mon. Wea. Rev.*, **143**, 536–562.

Shelton, K. L., and J. Molinari, 2009: Life of a six-hour hurricane. *Mon. Wea. Rev.*, **137**, 51-67.

Steranka, J., E. B. Rodgers, and R. C. Gentry, 1986: The Relationship between Satellite Measured Convective Bursts and Tropical Cyclone Intensification. *Mon. Wea. Rev.*, **114**, 1539–1546.

Stevenson, S. N., K. L. Corbosiero, and J. Molinari, 2014: The Convective Evolution and Rapid Intensification of Hurricane Earl (2010). *Mon. Wea. Rev.*, **142**, 4364–4380.Tao, D., and F. Zhang, 2014: Effect of environmental shear, sea-surface temperature, and ambient

moisture on the formation and predictability of tropical cyclones: An ensemble-mean perspective. *J. Adv. Model. Earth Syst.*, **6**, doi:10.1002/2014MS000314.

Stewart, S. R., 2014: Hurricane Edouard (AL062014). NHC Tropical Cyclone Report, 19 pp., available at http://www.nhc.noaa.gov/data/#tcr.

Wick, Gary. 2015. Hurricane and Severe Storm Sentinel (HS3) Global Hawk AVAPS Dropsonde System. Dataset available online [https://hs3.nsstc.nasa.gov/pub/hs3/AVAPS/] from the NASA Global Hydrology Resource Center DAAC, Huntsville, Alabama, U.S.A. doi: http://dx.doi.org/10.5067/HS3/AVAPS/DROPSONDE/DATA201.

Willoughby, H. E., F. D. Marks, and R. J. Feinberg, 1984: Sta- tionary and moving convective bands in hurricanes. *J. Atmos. Sci.*, **41**, 3189–3211, doi:10.1175/1520-0469(1984)041,3189: SAMCBI.2.0.CO;2.

Table Captions

Table 1. Instrument characteristics for the environmental and over-storm GH payloads.

Table 2. Summary of HS3 flights. AV=Air Vehicle. TS=Tropical Storm. TD=Tropical Depression. ET=Extratropical. NPP=NPOES Preparatory Project. MDR=Main Development Region.

Table 3. Table 3. NOAA P-3 and NASA GH dropsonde data near or within the eye of Edouard during 14-15 September. Time is given as the time of dropsonde release from the aircraft. WS150 is the wind speed averaged from the surface to 150 m altitude. Column 5 gives the number of observations used to calculate WS150 and the average geopotential height of the data points. Wind speeds are reduced to 10 m (WS10) from the average geopotential height following Table 3 of Franklin et al. (2003).

Figure Captions

Figure 1. Graphic summary of the HS3 Atlantic tropical cyclone and SAL flights. Panels show GH flight tracks for the (a) 2012 campaign, (b) 2013 campaign, and (c) 2014 campaign, while (d) shows the 2014 WB-57f flight tracks over Hurricane Gonzalo.

Figure 2. Figure 2. (a and b) Dropsonde-measured 800 hPa and 400 hPa relative humidity (with respect to water) and (c) 200 hPa temperature (colored circles) from the 11-12 September 2014 flight. Color bars for relative humidity and temperature are shown along the bottom of the figure. Wind barbs (full barb, 5 m s^{-1}; half-barb, 2.5 m s^{-1}; flags, 25 m s^{-1}) show storm-relative winds at the respective altitudes. Dropsonde locations account for dropsonde drift and storm motion, with positions adjusted to a reference time of 0900 UTC 12 September. Data superimposed on GOES infrared imagery (IR) at 0845 UTC and SSMI/S 91 GHz polarization corrected temperature [color scale in (b)] at 0849 UTC 12 September. (d-f) Same as (a-c), but for a reference time of 0032 UTC 15 September and superimposed on GOES IR imagery at 0045 UTC 15 September. Satellite imagery is from the Naval Research Laboratory Tropical Cyclone web page (http://www.nrlmry.navy.mil/TC.html).

Figure 3. GOES Infrared imagery (see color scale at bottom) from the Naval Research Laboratory tropical cyclone website for (a) 1115, (b) 1515, (c) and 2115 UTC 14 September; and (d) 0045, (e) 0315, and (f) 1315 UTC 15 September 2014. Flight segments associated with the center overflights at 2104 UTC 14 September and 0032 UTC 15 September are indicated by black lines in panels (c) and (d), respectively. The red portion of the flight segment in (d) corresponds to the period of the CPL and S-HIS data in Fig. 6.

Figure 4. (a) NOAA P-3 tail-Doppler radar analysis composite for 1500 UTC 14 September. Ground-relative wind speeds are shaded while radar reflectivity is contoured at 20, 25, and 30 dBZ values. Purple circles show range rings at approximately 25 and 50 km radius. (b) TRMM rainfall rates at 0044 UTC 15 September. Purple circles with the same radii as in (a) are aligned with precipitation features in the TRMM data.

Figure 5. (a) S-HIS brightness temperatures (color shading, K) for the 895-900 cm^{-1} channel. The eye of Edouard is labeled "Eye" near the warm brightness temperatures associated with the low clouds in the eye. The black dashed line shows the approximate flight path (line segments through dropsonde points only). Short curved line segments indicate dropsonde horizontal trajectories, with the release point coinciding with the flight path. Dropsonde times (UTC) are indicated. (b) Storm-relative tangential and (c) radial velocity, and (d) relative humidity with respect to water for temperatures ≥273.15K and with respect to ice at colder temperatures (color shading) from dropsonde data between 1935-2207 UTC 14 September. Dropsonde locations are indicated by vertical lines. Grey shading in right panels shows CPL attenuated backscatter (ABS, km^{-1} sr^{-1}) multiplied by 100. Vertical arrow in (b) indicates the location of the center dropsonde at 2104 UTC.

Figure 6. CPL attenuated backscatter (×100) and S-HIS real-time retrieved air temperature for the period 0020-0045 UTC 15 September during a transit over the storm from northeast to southwest of the center. Vertical dashed line shows the location of the 0032 UTC 15 September dropsonde. Each minute corresponds to approximately 10 km of distance.

Figure 7. Time series of NHC best-track (black line) central pressure and operational intensity estimates (red circles, from satellite and aircraft). Black circles indicate surface pressures from P-3 (filled circles) and GH (open circles) dropsondes. Blue lines indicate minimum central pressure estimates from the Holland (1980) equations for radii of 10, 15, and 20 km. Orange and purple lines along the bottom of the figure indicate on-station times for NOAA P-3s and GH, respectively. Text indicates significant events during storm evolution.

Figure 8. MODIS daily cloud and aerosol optical depth (colors) images show the evolution of the SAL outbreak near Hurricane Nadine on the indicated days. The flight track for the 11-12 September flight is shown in (b) and for the 14-15 September flight in (e). The black dashed line along the 11-12 September flight track in (b) indicates the time span of the data shown in Fig. 9. MODIS imagery obtained from the NASA Worldview web page (https://earthdata.nasa.gov/labs/worldview/).

Figure 9. (a) CPL aerosol backscatter ($\times 100$ km^{-1} sr^{-1}) showing the dust layer north of Nadine along the northern portions of the 5th and 6th north-south oriented flight legs (from left to right in Fig. 8b) during the 11-12 September 2012 flight. S-HIS (b) relative humidity with respect to water and (c) temperature perturbation for the same flight segment. Temperature perturbations are derived by removing the average temperature from 2000 UTC 11 September to 0600 UTC 12 September. The horizontal line marks the top of the dust layer, and the vertical lines separate times of nearly clear skies (0100-0149 UTC) from times with upper-level cloud cover. There is a reversal in the temperature anomalies below 400 hPa and much higher low-level relative humidity before 0100 UTC and after 0149 UTC, suggesting possible retrieval biases caused by upper-level clouds. Vertical arrows indicate the times of aircraft turns, first from northbound to eastbound, second from eastbound to southbound.

Figure 10. Equivalent potential temperature (colored circles) and storm-relative wind barbs (full barb, 5 m s^{-1}; half-barb, 2.5 m s^{-1}; flags, 25 m s^{-1}) at (a) 800 hPa and (b) 400 hPa superiposed on the GOES infrared imagery at 0015 UTC 15 September 2012. Dropsonde locations account for dropsonde drift and storm motion, with positions adjusted to a reference time of 0000 UTC 15 September. Color bars indicate θ_e values (K) corresponding to the dropsonde data in each panel. The orange line in (a) indicates the boundary of the SAL based upon dropsonde profiles.

Figure 11. Plots of (a) bulk Richarson number and CPL attenuated backscatter ($\times$100 km^{-1} sr^{-1}), (b) Brünt-Vaisala frequency, N^2 (s^{-2}), and (c) vertical wind shear, S (s^{-1}), for the Edouard cross section shown in Fig. 5. In (a), the 45% relative humidity contour is shown to indicate an approximate boundary of very dry air. In (b), contours are of potential temperature at 4 K intervals while in (c) contours show outflow regions with radial velocity at 4 m s^{-1} intervals starting at 4 m s^{-1}.

Figure S1. Hurricane Gonzalo on 17 September 2014 as observed from the HIWRAP Ka-band frequency as the storm was approaching Bermuda. Vertical cross section (top) and horizontal cross sections at 2.7, 5.0 and 7.3 km altitude (bottom panels) reconstructed from HIWRAP conical scanning outer beam. Both inner and outer eyewalls are observed at 110 and 160 km, and 40 and 250 km, respectively. The Ka-band data shown has higher resolution than the Ku-band and is more sensitive to light precipitation at upper levels in the eyewall, but suffers more attenuation in heavy rain near the surface.

Table 1. Instrument characteristics for the environmental and over-storm GH payloads.

Instrument	Spectral Bands	Spatial Resolution (FOV), Profile Resolution	Retrieved Measurement Precision	Data Products
Environmental Payload				
CPL	355, 532, and 1064 nm, with depolarization at 1064 nm	100 mr, 30 m vertical	Optical depth, 11-25%	Profiles of calibrated attenuated backscatter; cloud/aerosol layer boundaries; cloud/aerosol optical depth, extinction, and depolarization; color ratio
AVAPS	N/A	N/A, 0.5 s vertical	N/A	Quality controlled vertical profiles of temperature, pressure, humidity, wind speed and direction
S-HIS	Continuous spectral coverage 3.3 to 16.7 um @ 0.5 cm-1	0.1 radians (11 samples cross track), 1-3 km vertical	Temperature < 1K, water vapor < 15%	IR temperature spectra, IR cloud-top temperature, cloud-top height, cloud optical depth, cloud effective radius, water skin temperature. Atmospheric temperature and water vapor profiles in clear-sky conditions
Over-Storm Payload				
HAMSR	8 channels between 50-60 GHz, 10 between 113-118 GHz,	2 km horizontal, 1-3 km vertical	2 K for temperature, 15% for water vapor, 25% for	Calibrated geolocated brightness temperatures; vertical profiles of temperature, water vapor, and liquid water; precipitation

	and 7 between 166-183 GHz		liquid water	structure
HIRAD	4, 5, 6, 6.6 GHz	Horizontal resolution of 1.6 km (6.6 GHz) to 2.5 km (4 GHz) at nadir from 20 km altitude	1-5 m s^{-1} for wind speed	Brightness temperatures at 4 C-band frequencies; surface wind speed, rain rate
HIWRAP	13.35, 13.91, 33.72, 35.56 GHz	0.42 km (Ka) and 1.0 km (Ku) horizontal, 60 m vertical	Horizontal winds, < 2 m s^{-1}	Calibrated reflectivity, platform-corrected Doppler velocity, surface return, 3-D reflectivity fields and horizontal winds, ocean surface winds

Table 2. Summary of HS3 flights. AV=Air Vehicle. TS=Tropical Storm. TD=Tropical Depression. ET=Extratropical. NPP=NPOES Preparatory Project. MDR=Main Development Region.			
Date	**GH**	**Storm/Event**	**Description/comments**
2011			
8-9 Sep	AV-6	Pacific atmos. river	North-south cross section from 50° to 10°N along 154°W for intercomparison of AVAPS, S-HIS, and HAMSR.
13-14 Sep	AV-6	No storm	Intercomparison of AVAPS and NOAA G-IV dropsondes in warning area off Tampa, FL.
2012			
6-7 Sep	AV-6	Hurr. Leslie	Outflow structure of Leslie during transit to WFF.
11-12 Sep	AV-6	TS Nadine	Nadine beame a TS with SAL air along northern side. AVAPS failed mid-way through flight. Reduced CPL sensitivity due to cold instrument temperature.
14-15 Sep	AV-6	Hurr. Nadine	Nadine became a hurricane in high-shear conditions, SAL air wrapped partly around northern side. Reduced CPL sensitivity due to cold instrument temperature.
19-20 Sep	AV-6	TS Nadine	Nadine weakened to TS strength near the Azores. CPL issue resolved.
22-23 Sep	AV-6	TS Nadine	Nadine became a TS again after 1 day post-tropical.
26-27	AV-6	TS Nadine	Nadine moved southward, convection intensified 2 days prior

Sep			to re-intensification to hurricane strength.
6 Oct	AV-6	No storm	Underflew both NPP and Aqua, no dropsondes available.
5-6 Nov	AV-1	ET Cyclone	Test flight of AV-1 in an extratropical cyclone in the Pacific.
2013			
20-21 Aug	AV-6	Ex-Erin/SAL	Environmental sampling of shallow former TS Erin and SAL air mass. AVAPS released only 15 of 44 planned drops after it lost power from the aircraft.
24-25 Aug	AV-6	SAL	SAL flight in weak African wave disturbance.
29-30 Aug	AV-6	Pre-Gabrielle	Pre-Gabrielle African wave with SAL air.
3-4 Sep	AV-1	Pre-Gabrielle	Measurement of convective structure of Pre-Gabrielle and adjacent convective disturbance.
4-5 Sep	AV-6	TS Gabrielle	Environmental sampling of TS Gabrielle and adjacent convective disturbance.
7-8 Sep	AV-6	Ex-Gabrielle	Potential redevelopment of former TS Gabrielle.
15-16 Sep	AV-1	Hurr. Ingrid	Precipitation/wind measurements in Hurr. Ingrid. Flight cut short due to cold fuel temperatures.
16-17 Sep	AV-6	TS Humberto	Redevelopment of TS Humberto. Hybrid low-level warm-core/upper-level cold-core structure observed.
19-20	AV-6	Invest A95L	Environmental measurements of Invest A95L that, despite a

Sep			good low-level circulation and moisture, failed to develop into a tropical depression.
25 Sep	AV-1	ET cyclone	Precipitation system sampling in coordination with NOAA43 for HIWRAP/IWRAP intercomparison.
2014			
26-27 Aug	AV-6	Hurr. Cristobal	AV-6 transit and science flight over Hurricane Cristobal.
28-29 Aug	AV-6	Hurr. Cristobal	Hurricane Cristobal extratropical transition.
2-3 Sep	AV-6	TS Dolly	TS Dolly just prior to landfall along Mexican coast.
5-6 Sep	AV-6	SAL A90L	Invest A90L and its interaction with the SAL.
11-12 Sep	AV-6	TD6/TS Edouard	TS stage with possible nascent eye. CPL data loss due to disk failure.
14-15 Sep	AV-6	Hurr. Edouard	Four overflights near the center, rapid intensification.
16-17 Sep	AV-6	Hurr. Edouard	Mature stage, beginning of secondary eyewall replacement.
18-19 Sep	AV-6	Hurr./TS Edouard	Rapid weakening just west of the Azores.
22-23 Sep	AV-6	MDR Survey	Box from 60° to 21.5°W, eastbound at 19°N, westbound at 14°N.

28-29 Sep	AV-6	MDR Survey	Zig-zag pattern between 55°-27°W, 13-18°N.
30 Sep	AV-6	No storm	Intercomparison of AVAPS and G-IV dropsondes and flight-level winds during GH transit to AFRC.
15 Oct.	WB-57f	Hurr. Gonzalo	Two overpasses of Cat 3 intensity storm.
16 Oct.	WB-57f	Hurr. Gonzalo	Three overpasses of Cat 4 intensity storm.
17 Oct.	WB-57f	Hurr. Gonzalo	Two overpasses of Cat 3-4 intensity storm.

Table 3. NOAA P-3 and NASA GH dropsonde data near or within the eye of Edouard during 14-15 September. Time is given as the time of dropsonde release from the aircraft. WS150 is the wind speed averaged from the surface to 150 m altitude. Column 5 gives the number of observations used to calculate WS150 and the average geopotential height of the data points. Wind speeds are reduced to 10 m (WS10) from the average geopotential height following Table 3 of Franklin et al. (2003).

Aircraft/ Day/Time (UTC)	Release Location Relative to Center	P_{sfc} (hPa)	WS150 (m s^{-1})	# Obs/ GHT Avg. (m)	WS10 (m s^{-1})
P3/14/1500	Eye center	983	3	9	2.6
P3/14/1707	NE eye/eyewall	984	44	10/87	37
GH/14/2104	E eye/eyewall	972	48	16/85	41
GH/15/0032	Eye center	967	44	36/75	38
GH/15/0428	SE eye/eyewall	971	46	23/75	39

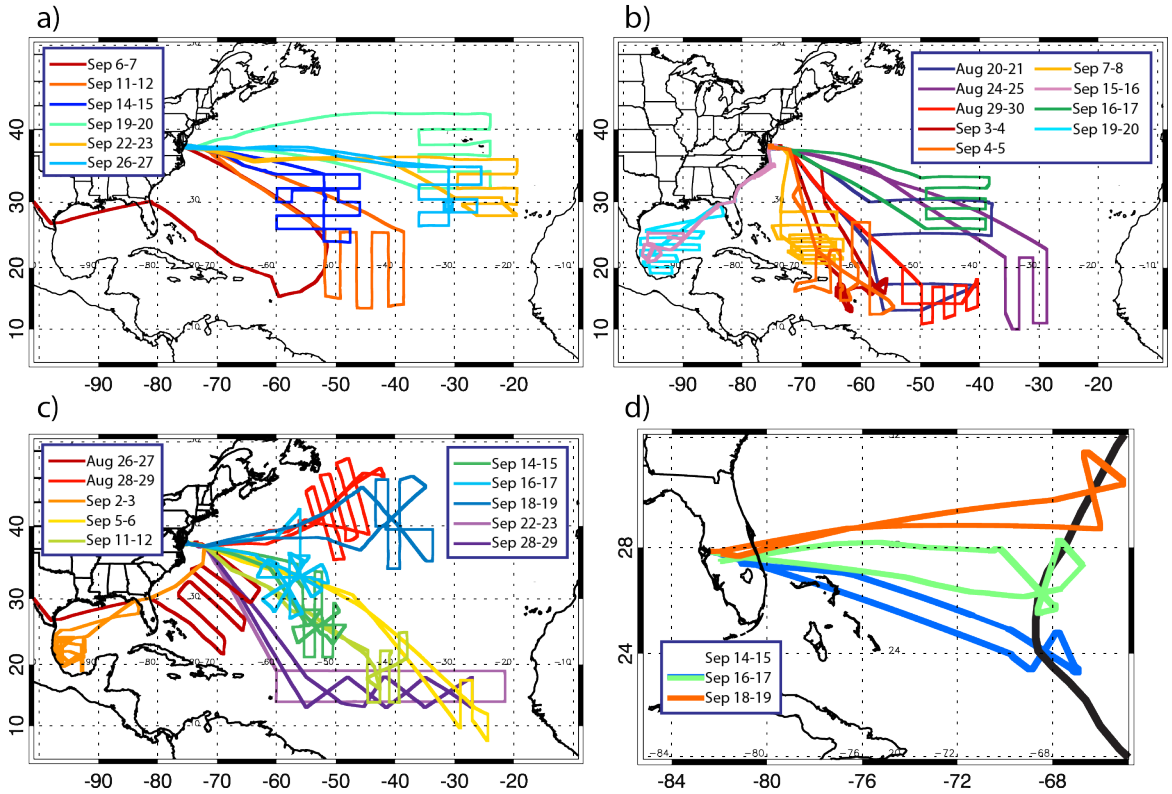

Figure 1. Graphic summary of the HS3 Atlantic tropical cyclone and SAL flights. Panels show GH flight tracks for the (a) 2012 campaign, (b) 2013 campaign, and (c) 2014 campaign, while (d) shows the 2014 WB-57f flight tracks over Hurricane Gonzalo.

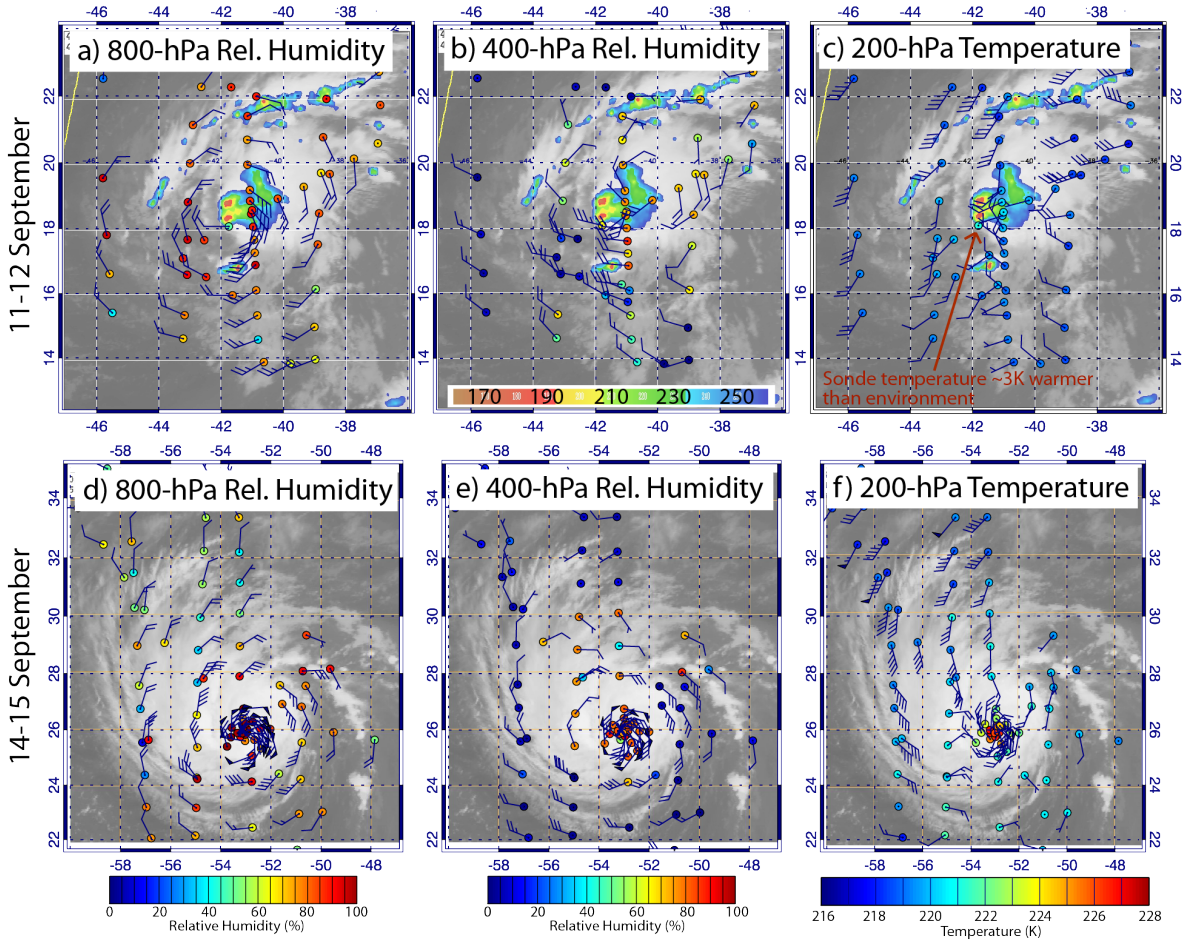

Figure 2. (a and b) Dropsonde-measured 800 hPa and 400 hPa relative humidity (with respect to water) and (c) 200 hPa temperature (colored circles) from the 11-12 September 2014 flight. Color bars for relative humidity and temperature are shown along the bottom of the figure. Wind barbs (full barb, 5 m s^{-1}; half-barb, 2.5 m s^{-1}; flags, 25 m s^{-1}) show storm-relative winds at the respective altitudes. Dropsonde locations account for dropsonde drift and storm motion, with positions adjusted to a reference time of 0900 UTC 12 September. Data superimposed on GOES infrared imagery (IR) at 0845 UTC and SSMI/S 91 GHz polarization corrected temperature [color scale in (b)] at 0849 UTC 12 September. (d-f) Same as (a-c), but for a reference time of 0032 UTC 15 September and superimposed on GOES IR imagery at 0045 UTC 15 September.

Satellite imagery is from the Naval Research Laboratory Tropical Cyclone web page (http://www.nrlmry.navy.mil/TC.html).

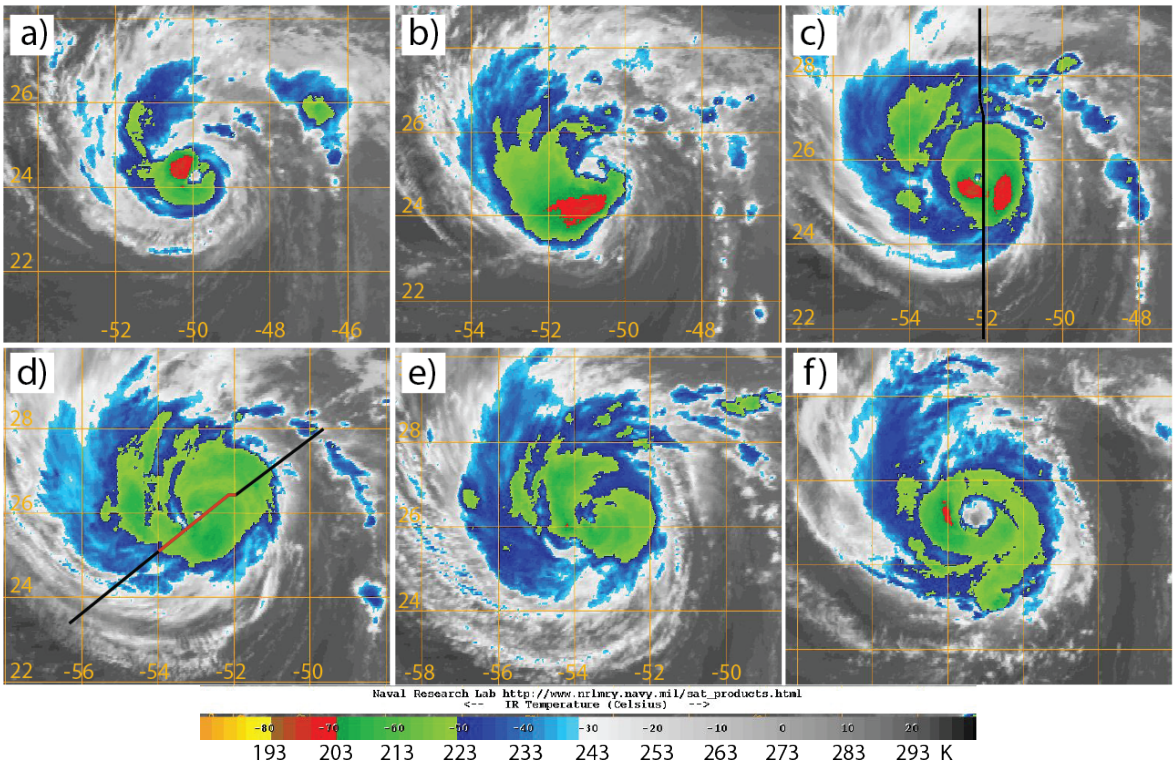

Figure 3. GOES Infrared imagery (see color scale at bottom) from the Naval Research Laboratory tropical cyclone website for (a) 1115, (b) 1515, (c) and 2115 UTC 14 September; and (d) 0045, (e) 0315, and (f) 1315 UTC 15 September 2014. Flight segments associated with the center overflights at 2104 UTC 14 September and 0032 UTC 15 September are indicated by black lines in panels (c) and (d), respectively. The red portion of the flight segment in (d) corresponds to the period of the CPL and S-HIS data in Fig. 6.

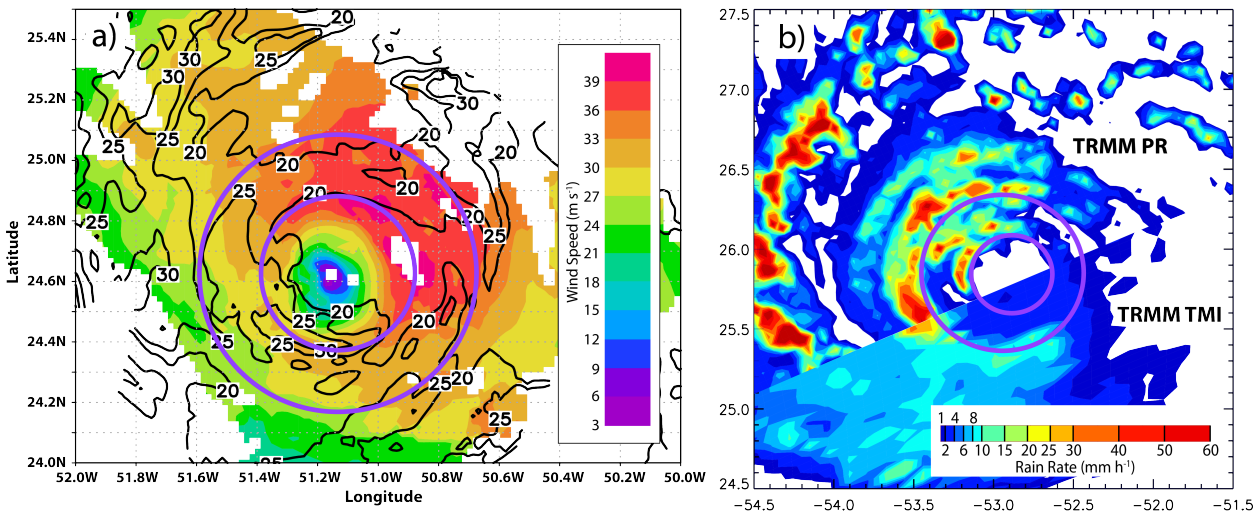

Figure 4. (a) NOAA P-3 tail-Doppler radar analysis composite for 1500 UTC 14 September. Ground-relative wind speeds are shaded while radar reflectivity is contoured at 20, 25, and 30 dBZ values. Purple circles show range rings at approximately 25 and 50 km radius. (b) TRMM rainfall rates at 0044 UTC 15 September. Purple circles with the same radii as in (a) are aligned with precipitation features in the TRMM data.

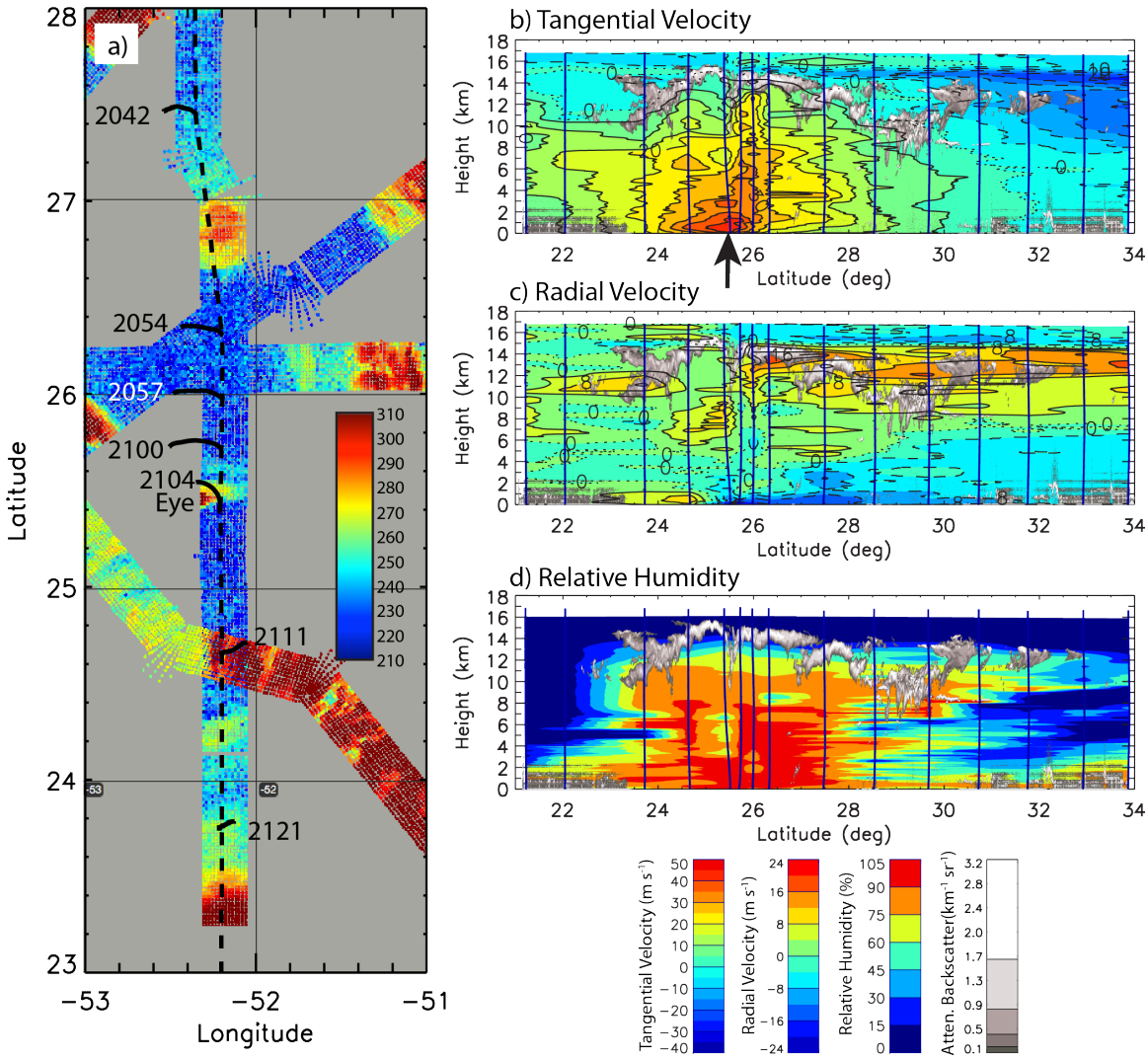

Figure 5. (a) S-HIS brightness temperatures (color shading, K) for the 895-900 cm^{-1} channel. The eye of Edouard is labeled "Eye" near the warm brightness temperatures associated with the low clouds in the eye. The black dashed line shows the approximate flight path (line segments through dropsonde points only). Short curved line segments indicate dropsonde horizontal trajectories, with the release point coinciding with the flight path. Dropsonde times (UTC) are indicated. (b) Storm-relative tangential and (c) radial velocity, and (d) relative humidity with respect to water for temperatures ≥273.15K and with respect to ice at colder temperatures (color

shading) from dropsonde data between 1935-2207 UTC 14 September. Dropsonde locations are indicated by vertical lines. Grey shading in right panels shows CPL attenuated backscatter (ABS, km^{-1} sr^{-1}) multiplied by 100. Vertical arrow in (b) indicates the location of the center dropsonde at 2104 UTC.

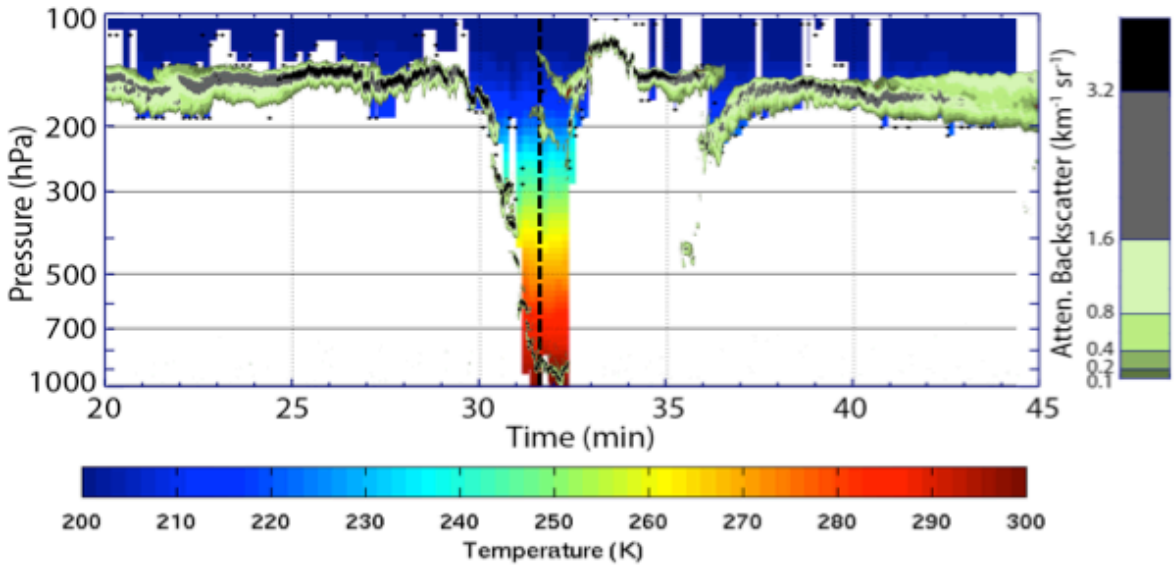

Figure 6. CPL attenuated backscatter (×100 km^{-1} sr^{-1}) and S-HIS real-time retrieved air temperature for the period 0020-0045 UTC 15 September during a transit over the storm from northeast to southwest of the center. Vertical dashed line shows the location of the 0032 UTC 15 September dropsonde. Each minute corresponds to approximately 10 km of distance.

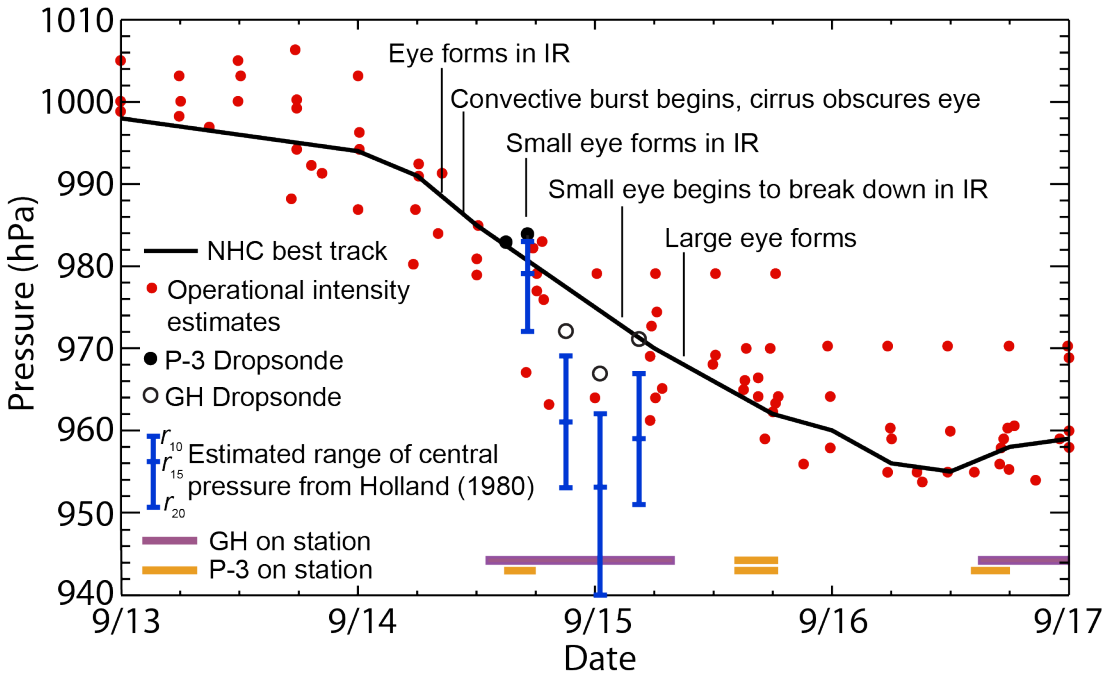

Figure 7. Time series of NHC best-track (black line) central pressure and operational intensity estimates (red circles, from satellite and aircraft). Black circles indicate surface pressures from P-3 (filled circles) and GH (open circles) dropsondes. Blue lines indicate minimum central pressure estimates from the Holland (1980) equations for radii of 10, 15, and 20 km. Orange and purple lines along the bottom of the figure indicate on-station times for NOAA P-3s and GH, respectively. Text indicates significant events during storm evolution.

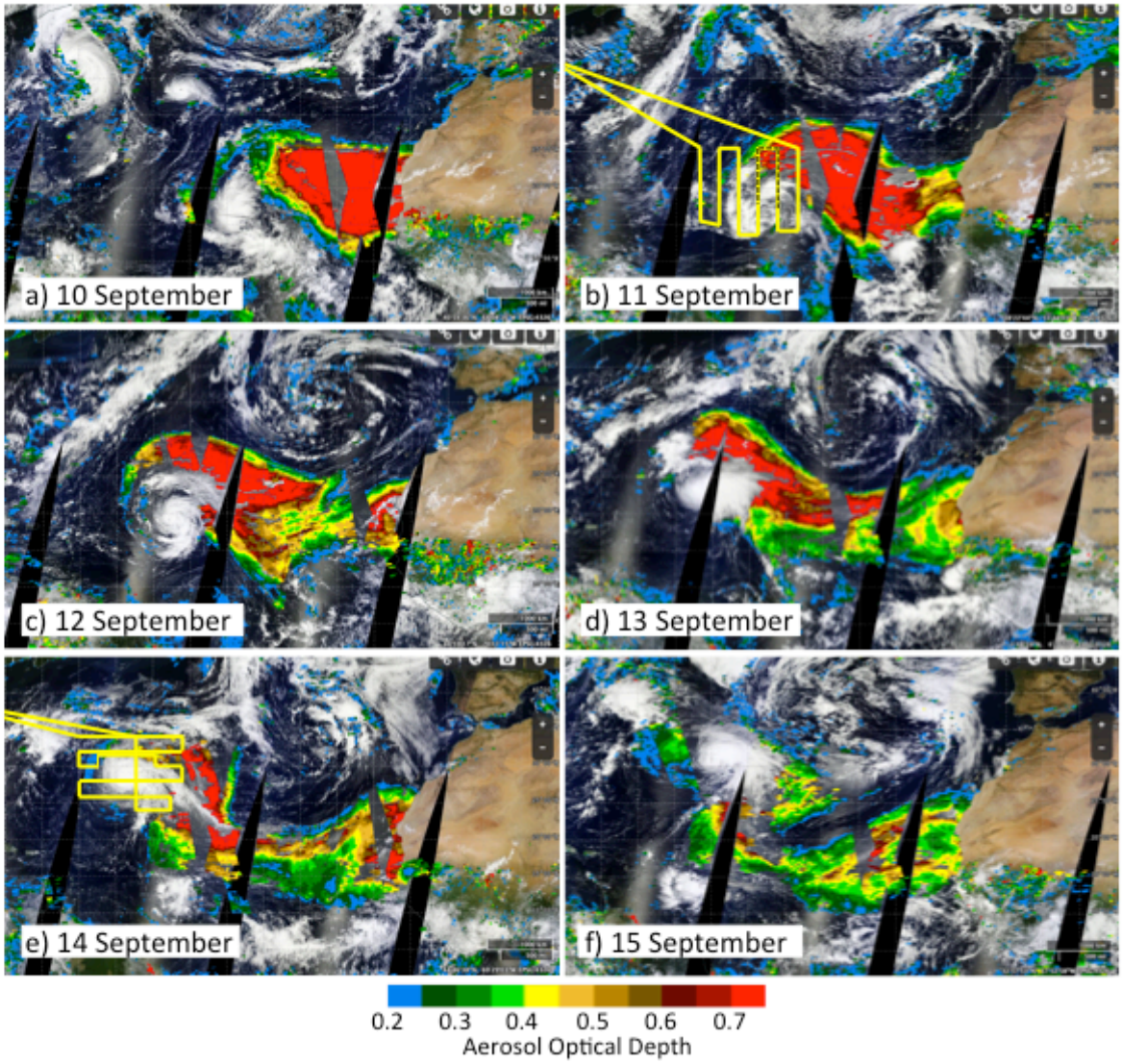

Figure 8. MODIS daily cloud and aerosol optical depth (colors) images show the evolution of the SAL outbreak near Hurricane Nadine on the indicated days. The flight track for the 11-12 September flight is shown in (b) and for the 14-15 September flight in (e). The black dashed line along the 11-12 September flight track in (b) indicates the time span of the data shown in Fig. 9. MODIS imagery obtained from the NASA Worldview web page (https://earthdata.nasa.gov/labs/worldview/).

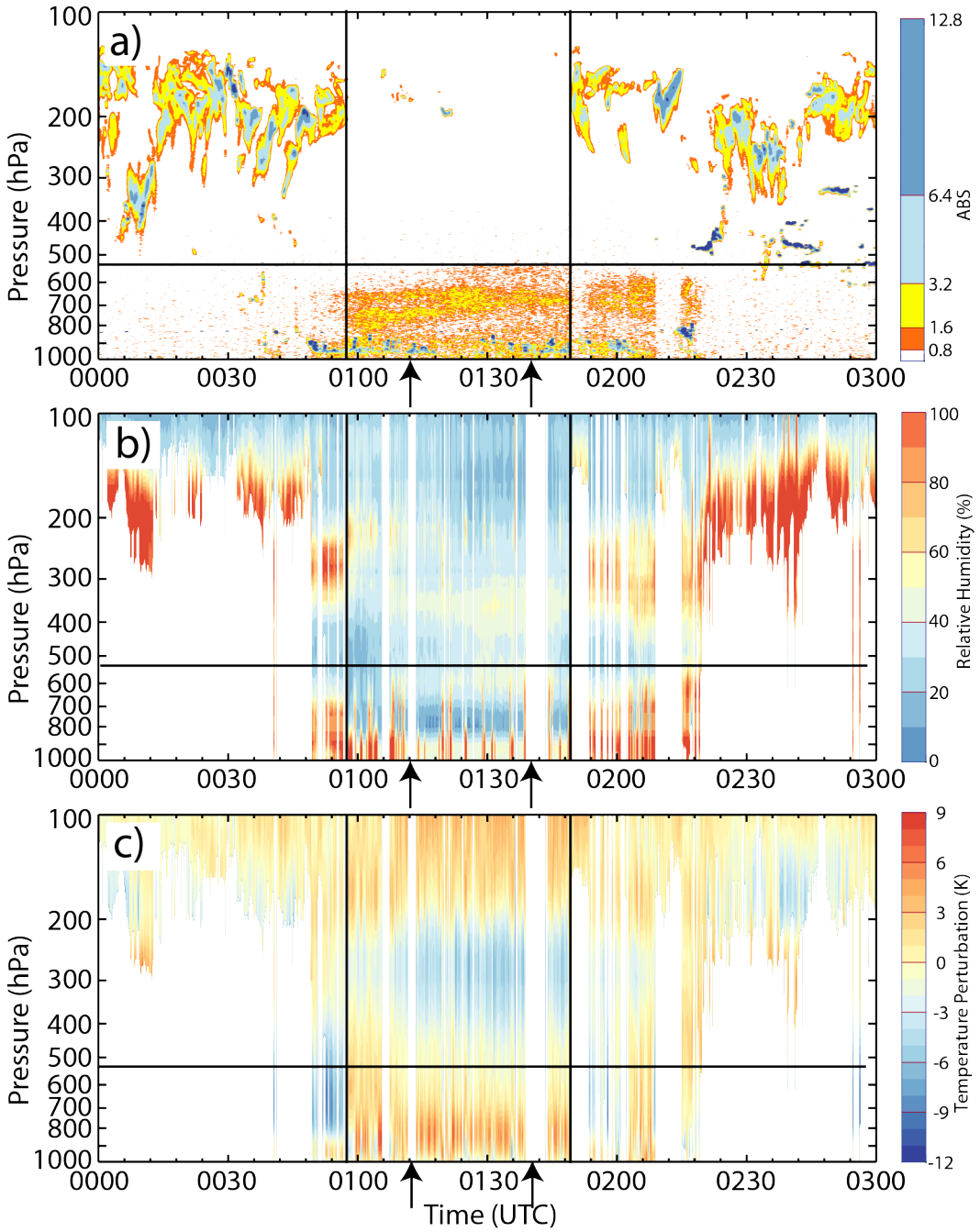

Figure 9. (a) CPL aerosol backscatter (×100 km^{-1} sr^{-1}) showing the dust layer north of Nadine along the northern portions of the 5th and 6th north-south oriented flight legs (from left to right in Fig. 8b) during the 11-12 September 2012 flight. S-HIS (b) relative humidity with respect to water and (c) temperature perturbation for the same flight segment. Temperature perturbations

are derived by removing the average temperature from 2000 UTC 11 September to 0600 UTC 12 September. The horizontal line marks the top of the dust layer, and the vertical lines separate times of nearly clear skies (0100-0149 UTC) from times with upper-level cloud cover. There is a reversal in the temperature anomalies below 400 hPa and much higher low-level relative humidity before 0100 UTC and after 0149 UTC, suggesting possible retrieval biases caused by upper-level clouds. Vertical arrows indicate the times of aircraft turns, first from northbound to eastbound, second from eastbound to southbound.

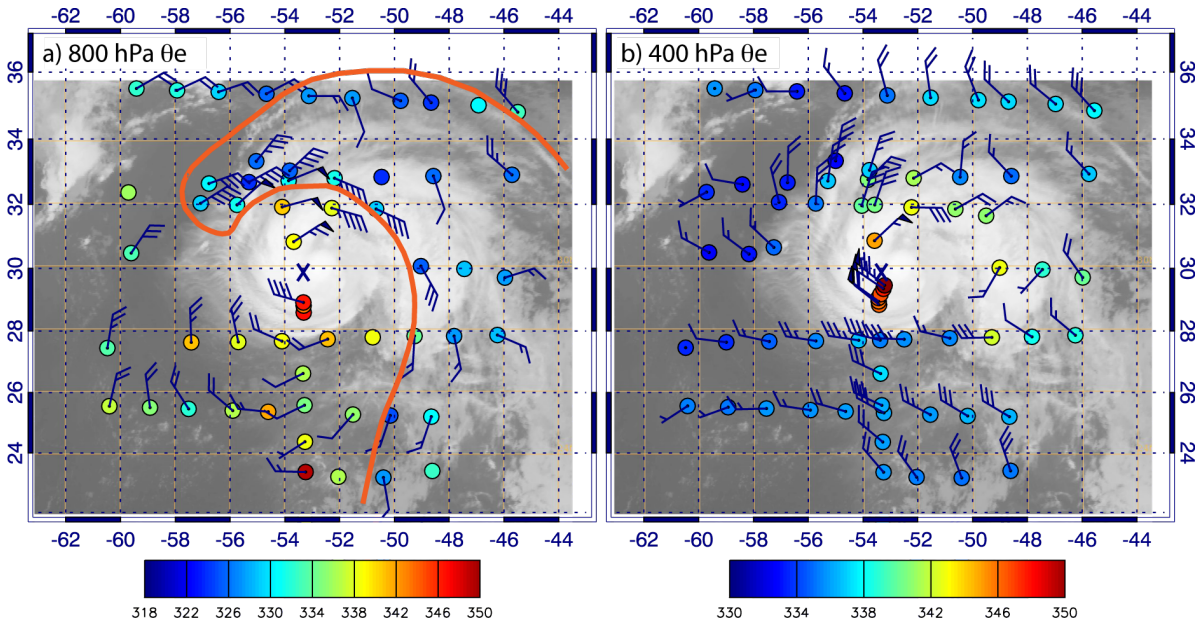

Figure 10. Equivalent potential temperature (colored circles) and storm-relative wind barbs (full barb, 5 m s^{-1}; half-barb, 2.5 m s^{-1}; flags, 25 m s^{-1}) at (a) 800 hPa and (b) 400 hPa superiposed on the GOES infrared imagery at 0015 UTC 15 September 2012. Dropsonde locations account for dropsonde drift and storm motion, with positions adjusted to a reference time of 0000 UTC 15 September. Color bars indicate θ_e values (K) corresponding to the dropsonde data in each panel. The orange line in (a) indicates the boundary of the SAL based upon dropsonde profiles.

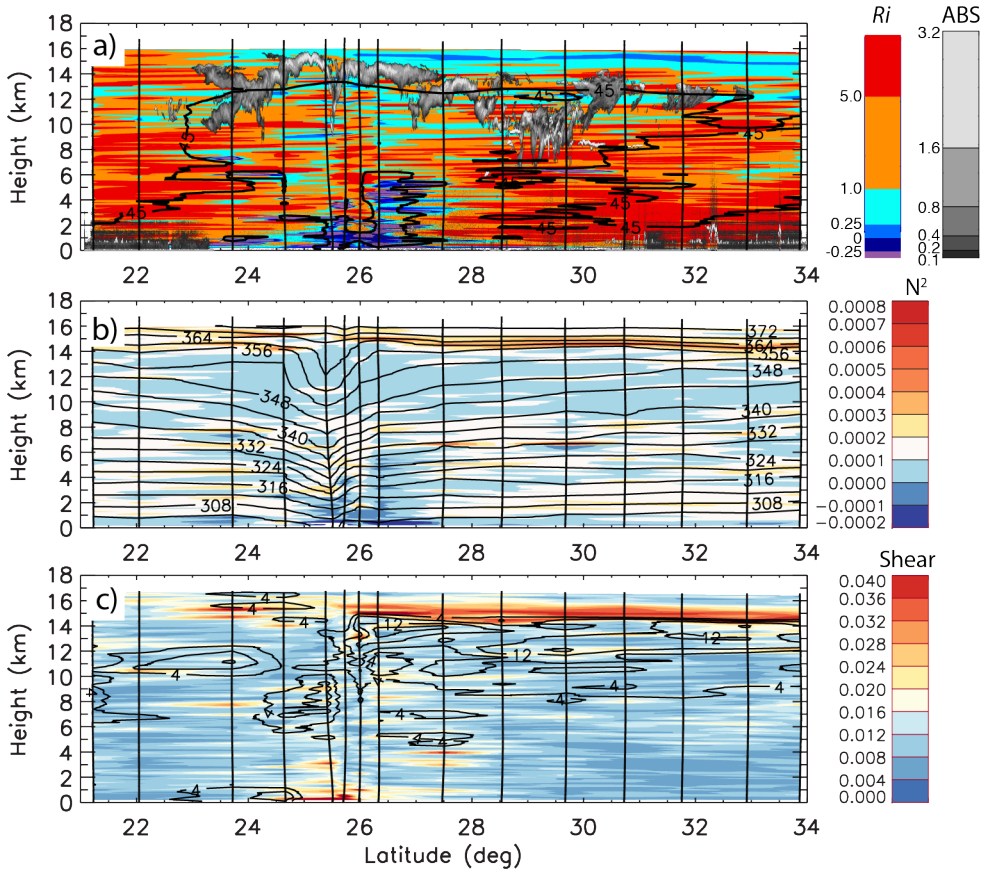

Figure 11. Plots of (a) bulk Richarson number and CPL attenuated backscatter (×100 km^{-1} sr^{-1}), (b) Brünt-Vaisala frequency, N^2 (s^{-2}), and (c) vertical wind shear, S (s^{-1}), for the Edouard cross section shown in Fig. 5. In (a), the 45% relative humidity contour is shown to indicate an approximate boundary of very dry air. In (b), contours are of potential temperature at 4 K intervals while in (c) contours show outflow regions with radial velocity at 4 m s^{-1} intervals starting at 4 m s^{-1}.

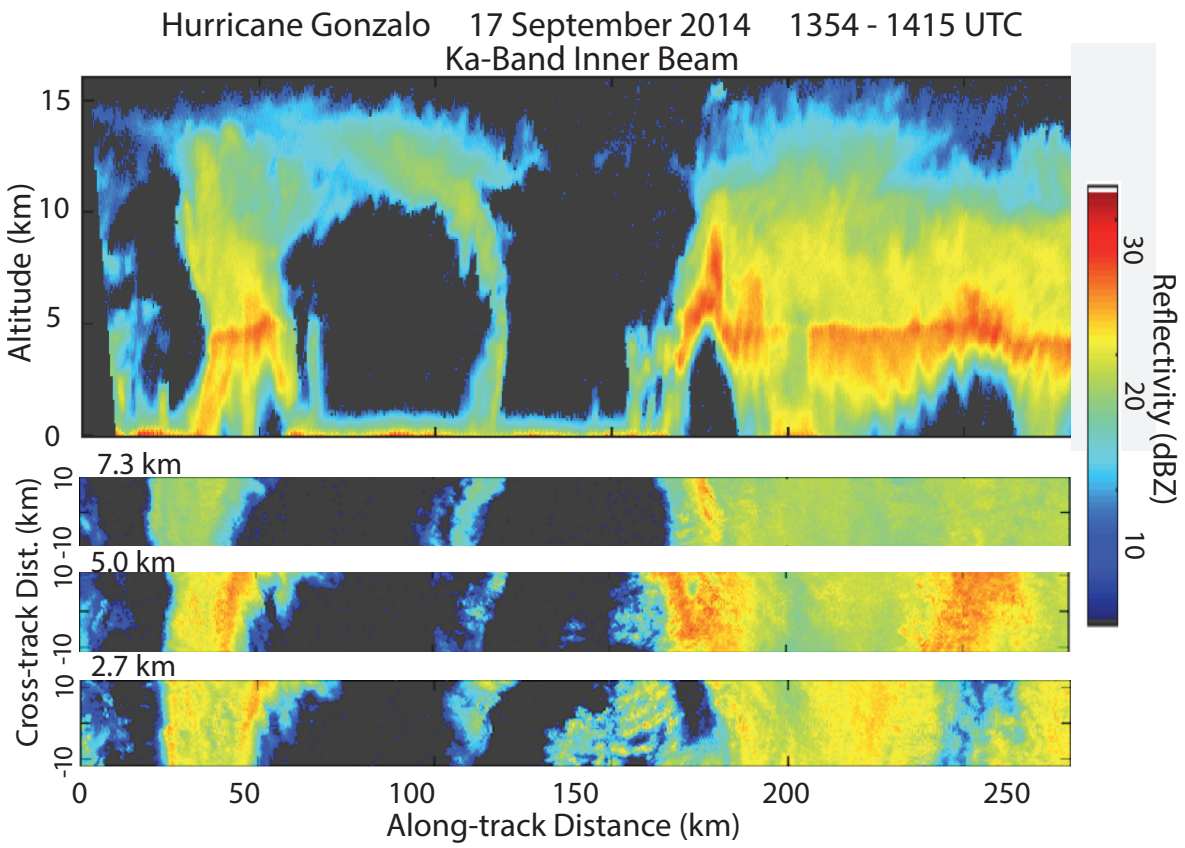

Figure S1. Hurricane Gonzalo on 17 September 2014 as observed from the HIWRAP Ka-band frequency as the storm was approaching Bermuda. Vertical cross section (top) and horizontal cross sections at 2.7, 5.0 and 7.3 km altitude (bottom panels) reconstructed from HIWRAP conical scanning outer beam. Both inner and outer eyewalls are observed at 110 and 160 km, and 40 and 250 km, respectively. The Ka-band data shown has higher resolution than the Ku-band and is more sensitive to light precipitation at upper levels in the eyewall, but suffers more attenuation in heavy rain near the surface.